

1 **Stability and Turbulence in the Atmospheric Boundary Layer: An Intercomparison**
2 **of Remote Sensing and Tower Observations**

3

4 KATJA FRIEDRICH¹, JULIE K. LUNDQUIST^{1,2}, MATTHEW AITKEN³, EVAN A. KALINA¹, AND

5 ROBERT F. MARSHALL¹

6

7

8 ¹*Department of Atmospheric and Oceanic Sciences,*

9 *University of Colorado, Boulder, CO*

10 ²*National Renewable Energy Laboratory,*

11 *Golden, CO*

12 ³*Department of Physics,*

13 *University of Colorado, Boulder, CO*

14

15

16 *Manuscript submitted electronically to*

17 *Geophysical Research Letters on*

18 *18 November 2011*

19

20 *Corresponding author address:*

21 *Dr. Katja Friedrich, ATOC, University of Colorado at Boulder, UCB 311, Boulder,*

22 *Colorado, CO 80309-0311, E-mail: Katja.Friedrich@colorado.edu, Phone:*

23 *+1.303.492.2041, Fax: +1.303.492.7167*

24 **Abstract**

25 When monitoring winds and atmospheric stability for wind energy applications, remote
26 sensing instruments present some advantages to *in-situ* instrumentation such as larger
27 vertical extent, easy installation and maintenance, measurements of vertical humidity
28 profiles throughout the boundary layer, and no restrictions on prevailing wind directions.
29 In this study, we compare remote sensing devices, Windcube lidar and microwave
30 radiometer, to meteorological *in-situ* tower measurements to demonstrate the accuracy of
31 these measurements and to assess the utility of the remote sensing instruments in
32 overcoming tower limitations. We also compare temperature and wind observations, as
33 well as calculations of Brunt-Väisälä frequency and Richardson numbers for the
34 instrument deployment period in May-June 2011 at the U.S. Department of Energy
35 National Renewable Energy Laboratory's Wind Center near Boulder, Colorado.
36 Differences in temperature and wind fall within the measurement accuracy of $\pm 0.1^\circ\text{C}$ for
37 temperature, $\sim 0.5 \text{ ms}^{-1}$ for wind speed and $\sim 1.3^\circ$ for wind direction. Although the tower-
38 radiometer intercomparison of the squared Brunt-Väisälä frequency shows a wide spread
39 ($\sim 3.2 \times 10^{-4} \text{ s}^{-2}$), the two approaches agree on the classification of conditions as stable,
40 neutral, or unstable in 94% of the cases. Differences in Richardson numbers from the *in-*
41 *situ* and remote sensing instruments show a spread of ~ 0.1 . We demonstrate that the
42 atmospheric stability is determined more accurately when the liquid-water mixing ratio
43 derived from the vertical humidity profile is considered under moist-adiabatic conditions.
44

45 **1. Introduction**

46 Wind anemometers and thermometers mounted on a tower have served as a
47 benchmark for meteorological observations at wind farms, despite being limited to a
48 height of 100 m. With the height limitation, towers can often not provide the observations
49 required for accurate wind measurements and forecasts, which are needed to satisfy the
50 rapid evolution of new wind turbine technologies. Moreover, tower measurements at
51 wind farms rarely include humidity, which is crucial to determining atmospheric stability
52 under near-saturated conditions. In this study, we demonstrate that combining a
53 Windcube lidar with a microwave radiometer provides measurements of wind and
54 temperature comparable to or better than those obtained from tower observations.
55 Furthermore, this combination overcomes the limits of traditional tower measurements by
56 collecting measurements well above tower heights. To our knowledge, this study is the
57 first time these instruments have been deployed and compared in this manner. While the
58 importance of humidity measurements has not yet been determined for wind farm
59 applications, we demonstrate that atmospheric stability is determined more accurately
60 when the liquid-water mixing ratio derived from the vertical humidity profile is
61 considered under moist-adiabatic conditions.

62 New wind turbine technologies and forecasting techniques require measurements at
63 heights beyond 100 m above ground level (AGL) [*Shaw et al. 2009*]. As power-
64 producing capacities have increased, turbine heights have grown from 60 m to 100 m
65 AGL for turbines with 1 MW to 2 MW capacity ratings to ~135 m AGL for turbines with
66 a 6-MW capacity rating [*Wiser and Bollinger, 2011*]. Several studies have emphasized
67 the importance of monitoring wind, wind shear, turbulence, and atmospheric stability not

68 just at hub heights, but also between the surface and ~1 km AGL to determine the amount
 69 of power that is generated by wind turbines [Kelley, 1994; Hand et al., 2003; Johnson et
 70 al., 2004; Barthelmie and Jensen, 2010; Politis et al., 2011; Wharton and Lundquist, 2011;
 71 Marquis et al. 2011, and references within]. The flexibility in deployment location and
 72 increase in vertical range at which measurements can be taken make the combination of
 73 remote sensing instruments more desirable than fixed meteorological towers with a
 74 limited vertical height.

75 Vertical profiles of moisture are generally not measured by *in-situ* tower instruments
 76 for wind farm applications [AWS Truepower, 2010]. As a result, atmospheric stability
 77 might not be correctly determined under moist-adiabatic conditions. The Richardson
 78 number compares the magnitude of buoyancy-driven forcing to shear-driven forcing:

$$79 \quad Ri = \frac{\frac{g d\bar{\theta}}{\bar{\theta} dz}}{\left(\frac{du}{dz}\right)^2 + \left(\frac{dv}{dz}\right)^2} = \frac{g \frac{d \ln \theta}{dz}}{\left(\frac{du}{dz}\right)^2 + \left(\frac{dv}{dz}\right)^2} = \frac{N_d^2}{\left(\frac{du}{dz}\right)^2 + \left(\frac{dv}{dz}\right)^2}, \quad (1)$$

80 where $\bar{\theta}$ represents mean potential temperature between the height z , θ the potential
 81 temperature, u and v the west-east and south-north wind components, respectively, g the
 82 acceleration due to gravity, and N_d^2 the squared Brunt-Väisälä frequency for an
 83 unsaturated atmosphere. In a saturated atmosphere, latent heat affects the temperature
 84 profile, and therefore a modification is required to Eq. (1) to incorporate the change in
 85 latent heat from condensation of water vapor [Einaudi and Lalas, 1973; Durran and
 86 Klemp, 1982], namely that the squared Brunt-Väisälä frequency (N_m^2) can be
 87 approximated following Einaudi and Lalas [1973] and Durran and Klemp [1982] as

$$88 \quad N_m^2 = g \left\{ \frac{1 + \frac{Lq_s}{RT}}{1 + \frac{\epsilon L^2 q_s}{c_p RT^2}} \left(\frac{d \ln \theta}{dz} + \frac{L}{c_p T} \frac{dq_s}{dz} \right) - \frac{dq_w}{dz} \right\}, \quad (2)$$

89 where L is the latent heat of vaporization, R is the ideal gas constant for dry air, and q_w ,
90 the total water mixing ratio, is the sum of the saturated mixing ratio (q_s) and the liquid
91 water mixing ratio (q_L), c_p is the heat capacity of dry air, ε is R/R_v , and R_v is the gas
92 constant for water vapor. Under dry-adiabatic conditions, there is no latent heat release
93 from condensation (i.e., $L = 0$), and the total water mixing ratio does not need to be
94 considered. In this case, Eq. (2) reduces to the dry-adiabatic squared Brunt-Väisälä
95 frequency, $N_d^2 = g \frac{d \ln \theta}{dz}$.

96

97 **2. Intercomparison experiment**

98

99 Simultaneous profiles of temperature, moisture, and wind were collected between
100 24 May–16 June 2011 by a Radiometrics MP-3000A microwave radiometer, an
101 NRG/Leosphere Windcube version 1 lidar, and sensors mounted on an 82-m
102 meteorological tower. The instruments were deployed in close proximity at the
103 Department of Energy’s National Renewable Energy Laboratory’s (NREL) Wind
104 Technology Center located ~ 5 km south of Boulder, Colorado. Three T-200A air
105 temperature probes were mounted on the meteorological tower (also referred to as the M2
106 tower) at a height of 2 m, 50 m, and 80 m above the ground. Temperature was measured
107 with an accuracy of $\pm 0.1^\circ\text{C}$ every 2 s and averaged over one minute. Wind was sampled
108 at 2 m, 5 m, 10 m, 20 m, 50 m, and 80 m using the Met One Instruments WS-201 wind
109 sensor system. The measurements were accumulated over one minute and had an
110 accuracy of $\pm 3.6^\circ$ for wind direction and $\pm 0.5 \text{ ms}^{-1}$ for wind speed. The wind direction

111 sensor at 80 m failed during this time period, and therefore wind directions from 80 m are
112 not included in this analysis.

113 Vertical profiles of temperature and relative humidity were provided by the
114 radiometer measuring microwave emission at 22 – 30 GHz (water vapor absorption band)
115 and 51 – 59 GHz (oxygen absorption band) and infrared emission at 9.6 – 11.5 microns.
116 Its zenith-pointing antenna yields a $\sim 6^\circ$ (22-30 GHz) and $\sim 3^\circ$ (51-59 GHz) beam
117 sampling width. Observations were integrated over 0.2 s, leading to a temperature
118 resolution of 0.25 K. Measurements were taken at zenith and at an elevation angle of 15°
119 above the ground, with the instrument pointing towards the north and south. Vertical
120 profiles of temperature and relative humidity were derived using a neural network
121 algorithm [Solheim *et al.*, 1998a, 1998b]. The algorithm, based on a radiative transfer
122 model [Rosenkranz, 1998], was trained on a 5-year radiosonde climatology from the
123 Denver, Colorado, National Weather Service sounding archive. The temperature and
124 moisture profiles ranged from the surface to 0.5 km AGL with 50 m vertical resolution,
125 0.5 km to 2 km AGL with 100 m resolution, and 2 km to 10 km AGL with 250 m
126 resolution. The radiometer was calibrated before the experiment using an external liquid
127 nitrogen target and an internal ambient target [Han and Westwater, 2000].

128 Approximately 1 km southeast of the radiometer and 1 km east of the M2 tower,
129 the Windcube lidar collected wind speed, wind direction, and turbulence intensity
130 profiles between 40 m and 200 m AGL; measurement levels were at 40 m, 50 m, 60 m,
131 and every 20 m from 60 m to 200 m AGL. Windcube version 1 is a pulsed lidar operating
132 at a wavelength of 1.5 μm . The fixed focus of the Windcube was optimized for minimum
133 error at 80 m AGL. As described in Courtney *et al.* [2008], the Windcube takes four slant

134 profiles at approximately 30° from the vertical and then averages those measurements
135 together to extract horizontal and vertical velocities from the measured radial components
136 of the flow, assuming horizontal homogeneity across the scanning cone for each
137 elevation. The diameter of this cone at 40 m AGL is ~ 46 m; at 200 m above the surface,
138 the diameter of the cone is ~ 230 m. The Windcube updates the wind speed after each
139 scan, which take place about once every second. Accordingly, there are approximately
140 600 wind speed measurements every 10 minutes. For a given 10-min interval, the average
141 wind speed and standard deviation are calculated based on these 600 measurements.
142 Turbulence intensity is the standard deviation of the wind speed divided by the average
143 wind speed over the 10 min interval. The Windcube's ability to discern wind speeds
144 depends on the particulate loading in the atmosphere, which influences the carrier-to-
145 noise ratio [Aitken *et al.*, 2011]. During this experiment, Windcube measurements were
146 accomplished up to 140 m 98.3% of the time during this collection period, and up to 200
147 m 77.5% of the time. As reported by Sathe *et al.* [2011], the mean error of the Windcube
148 in flat coastal conditions is within ± 0.05 m s⁻¹, with a standard deviation in mixed shear
149 conditions of about 0.15 m s⁻¹.

150

151 **3. Intercomparison between tower and remote sensing observations**

152 **3.1. Temperature**

153 Comparisons between temperature measurements from the microwave radiometer
154 and the *in-situ* tower observations (Fig. 1) provide an assessment of the utility of the
155 radiometer at the altitudes where the tower collected profiles. The temperature measured
156 by the radiometer was averaged between the 15° elevation scan pointing north and the

157 15° elevation scan pointing south. The averaged temperature from the radiometer was
158 compared to the tower observation taken within a time interval of ± 1 min. Radiometer
159 measurements are thus available at 50-m increments, and so the temperature “observed”
160 by the radiometer at 80 m was interpolated from the 50-m and 100-m observations. As
161 would be expected, the largest differences in temperature were observed at the surface
162 with a spread of 2.3°C (Fig. 1a) and a slight bias of -0.4°C (tower is cooler). The
163 differences in temperature decreased with distance from the surface as indicated by the
164 decrease in spread from 2.3°C at the surface to 1.4°C at 50 m (figure not shown) to 0.8°C
165 at 80 m (Fig. 1b). The median in temperature difference remained at ± 0.1 °C at 50 m and
166 80 m. The results from the tower-radiometer intercomparisons agree well with those of
167 other studies: for example, the root-mean square difference in temperature between
168 radiometers and radiosonde observations are < 1 °C below 500 m [*Guldner and Spänkuch*
169 *2001 and 2001; Liljegren et al., 2005; Cimini et al., 2006, 2007, 2009, and 2010;*
170 *Hewison 2007*].

171 The accuracy of the microwave radiometer can decrease rapidly during
172 precipitation because zenith brightness temperature measurements (90° elevation angle)
173 can be saturated and microwave emission scattered. *Cimini et al. [2010]* analyzed the
174 performance of the same Radiometrics MP-3000A microwave radiometer during the
175 2010 Winter Olympics in Vancouver, Canada. They discovered that the retrievals from
176 off-zenith observations at the 15° elevation angle exhibit less scatter and no temperature
177 saturation, as compared to the zenith scans. Similar results were obtained from the tower-
178 radiometer intercomparison presented in Fig. 1, which contained more than 8 hours of
179 rain with maximum rainfall rates of ~ 8 mmh⁻¹. Temperature differences between tower

180 and radiometer were less than 1 K during the rain events, as indicated by the gray plus
181 signs in Fig. 1. We conclude that the radiometer elevation scans provide reliable
182 assessments of temperature even during precipitation events.

183

184 **3.2. Wind Speed**

185 To compare the tower wind observations with the Windcube lidar measurements, we
186 averaged the tower data were over 10 min. Unfortunately, the vane at 80 m AGL was
187 broken during the intercomparison period, so the analysis solely focused on the
188 measurements at 50 m AGL. Recognizing that the tower wind speed and direction
189 measurements are only reliable when they are not in the wake of the tower, we only
190 considered westerly flow cases when the wind speed was $> 3 \text{ ms}^{-1}$ (i.e., minimum wind
191 speed for turbines to operate) between 180° and 360° as measured both by the
192 anemometer and the Windcube lidar. The differences in wind speed between the lidar and
193 the anemometer at 50 m AGL were relatively small with a median of -0.3 ms^{-1} and a
194 spread of 1.2 ms^{-1} , as indicated in Fig. 2a. The Windcube observed slightly higher wind
195 speeds compared to the anemometer. The intercomparison of wind direction reveals a
196 median differences of 2.1° and a spread 10.1° . The location of the Windcube relative to
197 the tower was not established for the purpose of direct comparisons of tower and
198 Windcube measurements, but even with the 1-km distance between the sites, the
199 agreement is remarkably good.

200

201 **3.3. Brunt-Väisälä frequency**

202 The squared Brunt-Väisälä frequency quantifies buoyancy forces, indicating the
203 frequency at which an air parcel will oscillate when subjected to an infinitesimal
204 perturbation in a stably-stratified atmosphere. As a result of latent heat release due to
205 condensation and latent heat absorption due to evaporation, the effective squared Brunt-
206 Väisälä frequency is lower in a saturated atmosphere than in a dry atmosphere.
207 Conditional instability, in which the atmosphere is stable when dry and unstable when
208 saturated, is a very common phenomenon in the atmosphere. As a result, an unstable
209 saturated atmosphere might appear stable if the vertical profile of moisture is ignored. In
210 wind energy applications, several investigators have observed that atmospheric stability
211 influences turbine performance and turbine wake evolution [e.g., *Kelley, 1994*;
212 *Barthelmie and Jensen, 2010*; *Wharton and Lundquist, 2011*].

213 The 1-minute temperature profiles observed by the radiometer and tower
214 thermometers (between the surface and 80 m AGL) enable calculations of the squared
215 Brunt-Väisälä frequency (Eq. 2), and therefore, enables us to identify the buoyant forcing
216 between the surface and 80 m AGL (Fig. 3a). We calculated frequencies using the same
217 surface temperature measurement from the radiometer because the lowest tower
218 measurement available is at 2 m AGL, and a large temperature gradient is expected
219 between the surface and 2 m AGL (cf. Fig. 1a). The tower and the radiometer tend to
220 agree on the nature of the temperature profile. Only 5.6% of all time periods showed
221 disagreement: 1.3% of the time the radiometer suggested negative N_d^2 values (unstable)
222 while the tower suggested positive N_d^2 values (stable), while 4.3% of the time the
223 radiometer suggested positive N_d^2 values (stable) while the tower suggested negative N_d^2
224 values (unstable). When 10-minute averages of the temperature profiles were used

225 instead of one-minute averages, agreement improved, suggesting that the disagreement is
226 due to heterogeneity of the site rather than to systematic differences between the
227 instrument platforms (figures not shown).

228 To study the relevance of latent heat release on the atmospheric stability, we
229 calculated the squared moist Brunt-Väisälä frequency using Eq. 2 and included the
230 vertical profile of moisture from the radiometer during time periods when the relative
231 humidity was >90% either at the surface or at 50 m AGL, which accounts for 12% of the
232 data. During about 40% of the moist-adiabatic events (blue plus signs in Fig. 3a), the
233 radiometer observations using the moisture profile indicated negative N_m^2 (unstable),
234 while the tower measurements indicated positive N_d^2 (stable). These cases underscore the
235 importance of the moisture profiles: without moisture profiles, an incorrect assessment of
236 atmospheric stratification emerges. In section 4, we investigate how this conditional
237 instability affects turbulence near the surface during a cold front passage.

238

239 **3.4. Richardson number**

240 The Richardson number (Ri) compares buoyant forcing to shear forcing; negative
241 values indicate an unstable atmosphere while positive values indicate a stable
242 atmosphere. Herein, we calculate the Richardson number from vertical profiles of
243 potential temperature observed by the radiometer and the wind observations from the
244 Windcube between the surface and 50 m AGL following Eq. 1. We assumed the winds
245 were still at the surface ($u = v = 0$ ms⁻¹) following *Vickert and Mahrt [2004]* and *Mahrt*
246 *et al. [2010]*. We compared Ri calculations from the remote sensing instruments to the
247 Ri calculations but using *in-situ* tower observations, all averaged over 10-minutes to

248 match the Windcube measurements. As with the wind intercomparison in Fig. 2, only
249 winds in excess of 3 m/s^{-1} and between 180° – 360° are considered for the analysis.
250 Differences between the *in-situ* and remote sensing-based Ri values have median and
251 spread values of 3×10^{-4} and 9×10^{-2} , respectively. The smallest differences occurred for
252 small Ri within stable atmospheric conditions with considerable wind shear, while larger
253 differences occurred when $Ri > 0.3$ (Fig. 3b). The squared moist Brunt-Väisälä
254 frequency is included in the Ri calculations using the Windcube and radiometer
255 observations when the relative humidity at the surface or at 50 m AGL exceeds 90%
256 (blue plus signs in Fig. 3b), which accounts for 9% of the total data. During about 37% of
257 the events using N_m^2 , the Richardson numbers, calculated from the remote sensing
258 observations and the moisture profile information, were negative (unstable atmosphere),
259 while the tower measurements indicated a stable atmosphere with positive Richardson
260 numbers. These cases underscore the importance of the moisture profiles. In most of the
261 cases with moist adiabatic conditions, the atmospheric stability would be assessed
262 incorrectly using the tower conditions.

263

264 **3.5. Turbulence intensity**

265 Performance of wind turbines that is assessed using the turbulent intensity is also
266 sensitive to changes in atmospheric turbulence, which is a measure of the variation in
267 wind speed about the mean [*Kaiser et al. 2003; Honhoff 2007; Tindal et al. 2008;*
268 *Rareshide et al. 2009*]. Although most researchers prefer to use a three-dimensional
269 assessment of turbulent motions, many wind farms only deploy cup anemometers, so
270 turbulence intensity is often the only available estimate of turbulent motions. Turbulence

271 intensity is defined as the coefficient of variation, i.e., the ratio of the standard deviation
272 of the wind velocity to the mean wind velocity. Changes in the atmospheric stability in
273 the boundary layer are often correlated with large variations in turbulent intensity. Low
274 turbulence intensity is expected under stable conditions, while strong mixing during
275 unstable conditions will increase the turbulence intensity. Herein, we calculated the
276 turbulence intensity using wind observations from the Windcube lidar and compare those
277 values to the dry and moist Ri (Fig. 3c-d). High values of turbulence intensity were
278 observed when the atmosphere was unstable or neutral with negative dry Richardson
279 numbers and dry Richardson numbers close to zero, respectively. With increasing
280 stability, i.e., an increase in Ri , the turbulence intensity decreased. Under moist adiabatic
281 conditions (blue plus signs in Fig. 3c) turbulence intensity ranged between 0 and 0.7.
282 Using the dry Richardson number under moist-adiabatic conditions can lead to
283 inaccuracies, which are linked to high values of turbulence intensity and increasing
284 positive Ri numbers. In the limited cases we explored, when Ri numbers were close to
285 zero, the relationship between turbulent intensity and Ri numbers were similar for dry-
286 and moist-adiabatic conditions.

287

288 **4. Richardson number during a cold front passage**

289 In this section, we analyze the impact of the vertical moisture profile on Ri during a
290 rain event. Figure 4 shows the Windcube and microwave radiometer observations during
291 a cold front passage on 9 June 2011. On that day, an upper-level trough passed over
292 Colorado with a surface cold front moving over the instruments at about 0820 UTC. Prior
293 to the cold front passage (0000-0820 UTC), the atmosphere below the mountain crests

294 was stable with a northerly surface wind of 5–15 ms⁻¹ (Fig. 4a, e). With a relative
295 humidity below 60%, the atmosphere was unsaturated and stable with turbulence
296 intensity values < 0.4. During the cold front passage, the surface temperature dropped by
297 ~10°C (Fig. 4b), relative humidity increased from 20% to 100% (Fig. 4c), wind veered to
298 the east for ~1 h and then returned to northwesterly winds with steady wind speeds of 15
299 ms⁻¹ (Fig. 4a). During the cold front passage, the atmosphere became neutral with
300 Richardson numbers around zero and remained neutral under both saturated and
301 unsaturated conditions, and turbulence intensity remained below 0.2 between 0820-1130
302 UTC. Note that the squared moist Brunt-Väisälä frequency was negative, while N_d^2
303 remained around zero. As a result, the Richardson numbers, which are similar for
304 saturated and unsaturated conditions, were governed by the wind shear. Between 1200-
305 1500 UTC, the atmosphere became slightly conditionally unstable, i.e., slightly
306 stable/neutral if dry-adiabatic conditions are assumed but unstable under moist-adiabatic
307 conditions (Fig. 4d). Accordingly, turbulence intensity slightly increased and ranged
308 between 0.2-0.6 (Fig. 4e). With relative humidity values >95%, the atmosphere was close
309 to being saturated during this time. Rain was observed at ~0430 UTC prior to the cold
310 front passage and occasionally at the surface between ~0820-1430 UTC (Fig. 4c). While
311 maintaining the wind speed, the wind direction backed to northerly after 2000 UTC.
312 Ceilometer observations from the nearby University of Colorado Skywatch Observatory
313 indicate the cloud base remained below ~100 m AGL until 2000 UTC (figure not shown).
314 The atmosphere became more unstable under both saturated and unsaturated conditions.
315 The calculation of the Brunt-Väisälä frequency and the Richardson number
316 underscore the critical role of latent heat release in understanding atmospheric stability

317 and turbulence. Even though rain only occurred occasionally after 0820 UTC, it can be
318 assumed, based on the low cloud height and the relative humidity exceeding 95%, that
319 the atmosphere was near-saturated. The differences between the Richardson numbers
320 using the dry and moist Brunt-Väisälä frequency increased to ~ 0.2 between 0820-1400
321 UTC. After 1400 UTC, the atmosphere became unstable under both dry and moist-
322 adiabatic conditions, and the Richardson number decreased for both *in-situ* and remote
323 sensing instruments.

324 The microwave radiometer observations also revealed important meteorological
325 structures, which are important to forecast the 3-dimensional structure of the atmosphere
326 and cannot be observed with tower observations. Prior to the cold front passage,
327 evaporation occurred below 1.5 km AGL, as indicated by a large gradient in relative
328 humidity. Upper-level dry-air intrusions, which occurred after 1300 UTC above 1 km
329 AGL, have been often been observed with the passage of an upper-level trough leading to
330 a destabilization of the atmosphere [*Schultz and Trapp 2003; Steenburgh 2003; Colle et*
331 *al. 2005*].

332

333 **5. Conclusion**

334 We examined the advantages of remote sensing of turbulence and stability within the
335 atmospheric boundary layer by comparing Windcube lidar and microwave radiometer
336 measurements to *in-situ* tower observations. The investigation focused on three main
337 issues: 1) the accuracy of wind and temperature measurements from the remote sensing
338 instruments, 2) advantages of remote sensing instruments for monitoring stability and

339 turbulence in the atmospheric boundary layer, and 3) the influence of the humidity profile
340 on atmospheric stability and Richardson number.

341 The Windcube lidar and Radiometrics microwave radiometer provided measurements
342 as accurate as the *in-situ* tower observations. Differences in temperature ranged between
343 0.7–1.7°C between the tower and radiometer. Slightly larger values were observed at the
344 surface, which were likely related to thermal turbulence rather than instrument accuracy.
345 Wind observations from the Windcube lidar and *in-situ* tower indicated a spread of 1.2
346 ms^{-1} for wind speed. As a result, the differences in squared Brunt-Väisälä frequency and
347 the Richardson numbers based on in-situ tower and remote sensing observations showed
348 median values of $0.2 \times 10^{-4} \text{ s}^{-2}$ and 0.0003 and spread values of $3.2 \times 10^{-4} \text{ s}^{-2}$ and 0.09,
349 respectively.

350 Mobility of the instruments, larger vertical extent of measurements, and ease of
351 maintenance are the main advantages of remote sensing instruments over tower
352 observations. With the remote sensing instruments used herein, temperature, moisture,
353 and wind measurements can be collected throughout the turbine rotor disk layer, even
354 when turbine hub heights reach as high as 135 m AGL. Further, characteristics of the
355 atmospheric boundary layer, including atmospheric stability and turbulence, can be
356 monitored above turbine height and be used for nowcasting and forecasting applications.
357 Wind measurements and, therefore, the calculation of Richardson numbers are not
358 limited to cases when the orientation of an anemometer is appropriate for the wind
359 direction but can instead be accomplished under any wind direction.

360 While the importance of humidity measurements has yet to be established for wind
361 energy applications, we demonstrated that the atmospheric stability, and therefore the

362 Richardson number, were determined more accurately when the liquid-water mixing ratio
363 derived from the vertical humidity profile was considered under moist-adiabatic
364 conditions. Under those conditions, the squared moist Brunt-Väisälä frequency derived
365 from the radiometer humidity profile indicated that the atmosphere was unstable, instead
366 of stable as indicated when using the squared dry Brunt-Väisälä frequency. In those
367 cases, changes in the squared Brunt-Väisälä frequency affected the accuracy of the
368 Richardson number and therefore, the relationship between the Richardson number and
369 the turbulence intensity.

370 This intercomparison study also showed the ability of the remote sensing
371 instruments in overcoming the limits of traditional tower measurements by measuring
372 wind, temperature and humidity beyond 100 m AGL. In addition, the small footprint of
373 the remote sensing instruments provides flexibility in choosing deployment locations.
374 Further observational studies are necessary to quantify the role of vertical humidity
375 profiles on the stability during moist-adiabatic conditions and to determine how humidity
376 impacts the formation and maintenance of low-level wind maxima and wind turbine
377 performance. The implementation of remote sensing observations throughout the entire
378 boundary layer, in particular the vertical profiles of humidity, into nowcasting and
379 forecasting procedures is necessary to investigate further the influence of those
380 measurements on improvements in wind turbine operations.

381

382

383 **Acknowledgments.** This work was supported in part by the National Renewable Energy
384 Laboratory under Prof. Lundquist's Joint Appointment. We thank Dr. Fort Felker, Mr.

385 Michael Stewart, Mr. David Simms, Ms. Brenda Crook, Mr. Salvador Aguirre, and Mrs.
386 Cynthia Szydlek for enabling the simultaneous deployment of these instruments at
387 NREL's National Wind Technology Center (NWTC). We thank Mr. Peter Horsager and
388 Mr. Michael Ashiem for their efforts in instrument maintenance and data collection and
389 Randolph Ware of Radiometrics for the fruitful discussions about this manuscript. The
390 Skywatch Observatory (<http://skywatch.colorado.edu>) was sponsored by the National
391 Science Foundation under grant 0837388. NWTC M2 meteorological tower data were
392 collected from http://www.nrel.gov/midc/nwtc_m2/.

393

394

395 **References**

- 396 Aitken, M. L., M. E. Rhodes, and J. K. Lundquist (2011), Performance of a wind-
397 profiling lidar in the region of wind turbine rotor disks. In review at *Journal of*
398 *Atmospheric and Oceanic Technology*.
- 399 AWS Truepower (2010), Wind resource assessment handbook. NYSERDA Report 10-30
400 (available online at
401 www.nysERDA.org/publications/wind_resource_assessment_handbook10_30.pdf)
- 402 Barthelmie, R. J., and L. E. Jensen (2010), Evaluation of wind farm efficiency and wind
403 turbine wakes at the Nysted offshore wind farm. *Wind Energy*, 13, 573-586.
- 404 Cimini, D., E. Campos, R. Ware, S. Albers, G. Giuliani, J. Oreamuno, P. Joe, S. E Koch,
405 S. Cober, and E. Westwater (2010), Thermodynamic atmospheric profiling during
406 the 2010 Winter Olympics using ground-based microwave radiometry. *IEEE*
407 *Transactions on Geoscience and Remote Sensing*, 99, 1-11.
408 doi:10.1109/TGRS.2011.2154337.
- 409 ———, E. R. Westwater, and A. J. Gasiewski (2009), Temperature and humidity
410 profiling in the Arctic using millimeter-wave radiometry and 1DVAR, *IEEE*
411 *Transactions on Geoscience and Remote Sensing*, 10.1109/TGRS.2009.2030500.
- 412 ———, ———, ———, M. Klein, V. Y. Leuski, and J. C. Liljegren
413 (2007), Ground-based millimeter- and submillimeter-wave observations of low
414 vapor and liquid water contents. *IEEE Transactions on Geoscience and Remote*
415 *Sensing*. 45(7), 2169-2180, doi: 10.1109/TGRS.2007.897450.
- 416 ———, T. J. Hewison, L. Martin, J. Gueldner, C. Gaffard, and F. Marzano (2006),
417 Temperature and humidity profile retrievals from ground-based microwave

418 radiometers during TUC, *Met. Z.*, 15, 45-56.

419 Colle, B. A., J. B. Wolfe, W. J. Steenburgh, D. E. Kingsmill, J. A.W. Cox, and J. C.
420 Shafer (2005), High-resolution simulations and microphysical validation of an
421 orographic precipitation event over the Wasatch Mountains during IPEX IOP3.
422 *Mon. Wea. Rev.*, 133, 2947-2971.

423 Courtney, M., R. Wagner, and P. Lindelow (2008), Testing and comparison of lidars for
424 profile and turbulence measurements in wind energy. Proc. 14th Int. Symp. for the
425 Advancement of Boundary Layer Remote Sensing, Vol. 1, Risø DTU, Denmark,
426 IOP Conference Series: Earth and Environmental Science, 012021.

427 Durran, D. R., and Joseph B. Klemp (1982), On the effects of moisture on the Brunt-
428 Väisälä frequency, *J. Atmos. Sci.*, 39, 2152-2158. doi:10.1175/1520-
429 0469(1982)039<2152:OTEOMO>2.0.CO;2.

430 Einaudi, F. and D. P. Lalas (1973), On the correct use of the wet adiabatic lapse rate in
431 stability criteria of a saturated atmosphere, *J. Appl. Meteor.*, 13, 318-324.

432 Güldner, J., and D. Spänkuch (2001), Remote sensing of the thermodynamic state of the
433 atmospheric boundary layer by ground-based microwave radiometry. *J. Atmos.*
434 *Oceanic Technol.*, 18, 925–933. doi: 10.1175/1520-
435 0426(2001)018<0925:RSOTTS>2.0.CO;2

436 Han Y, and E. R. Westwater (2000), Analysis and improvement of tipping calibration for
437 ground-based microwave radiometers. *IEEE Transactions on Geoscience and*
438 *Remote Sensing.* 38(3), 1260-1276, doi: 10.1109/36.843018.

439 Hand, M. M., N. D. Kelley, and M. J. Balas (2003), Identification of wind turbine
440 response to turbulent inflow structures. Proc. 4th ASME/JSME Joint Fluids

441 *Engineering Conference Honolulu, Hawaii, June 6–10, 2003.*

442 Hewison T. (2007), 1D-VAR retrievals of temperature and humidity profiles from a
443 ground-based microwave radiometer, *IEEE Transactions on Geoscience and*
444 *Remote Sensing*, 45, 2163-2168.

445 Honhoff S. (2007), Power Curves – The effect of environmental conditions, GE Wind,
446 AWEA Wind Speed and Energy Workshop, Portland, September.

447 Johnson, K. E., L. J. Fingersh, M. J. Balas, and L. Y. Pao (2004), Methods for increasing
448 region 2 power capture on a variable speed HAWT, *Paper No. AIAA-2004-0350,*
449 *Proc. 23rd ASME Wind Energy Symposium, Reno, NV*, pp. 103–113.

450 Kaiser K., H. Hohlen and W. Langreder (2003), Turbulence correction for power curves,
451 Proceedings of European Wind Energy Conference, EWEC, Madrid, Spain.

452 Kelley, N. D. (1994), The identification of inflow fluid dynamics parameters that can be
453 used to scale fatigue loading spectra of wind turbine structural components, *1994*
454 *ASME Wind Energy Symposium, AIAA/ASME*, pp. 181-196.

455 Mahrt, L. (2010), Variability and maintenance of turbulence in the very stable boundary
456 layer, *Boundary-Layer Meteorology*, 135, 1-18, DOI: 10.1007/s10546-009-
457 9463-6.

458 Marquis, M., J. Wilczak, M. Ahlstrom, J. Sharp, A. Stern, J. C. Smith, and S. Calvert
459 (2011), Forecasting the wind to each significant penetration levels of wind
460 energy, *Bull. Amer. Meteor. Soc.*, 92, 1159-1171, doi:
461 10.1175/2011BAMS3033.1.

462 Politis, E. S., J. Prospathopoulos, D. Cabezon, K. S. Hansen, P. K. Chaviaropoulos, and
463 R. J. Barthelmie (2011), Modeling wake effects in large wind farms in complex

464 terrain: the problem, the methods and the issues, *Wind Energy*. doi:
465 10.1002/we.481

466 Rareshide E., A. Tindal, C. Johnson, A. Graves, E. Simpson, J. Blegg, T. Harris, and D.
467 Schoborg (2009), Effects of complex wind regimes on turbine performance.
468 Proceedings of AWEA WINDPOWER Conference, Chicago, May 2009

469 Rosenkranz P. W. (1998), Water vapor microwave continuum absorption: A comparison
470 of measurements and models, *Radio Science*, 33, 919-928

471 Sathe, A., J. Mann, J. Gottschall, and M. S. Courtney (2011), Can wind lidars measure
472 turbulence? *J. Atmos. Oceanic Technol.*, 28, 853–868. doi: 10.1175/JTECH-D-10-
473 05004.1

474 Liljegren, J. C., S.-A. Boukabara, K. Cady-Pereira, and S. A. Clough (2005), The effect
475 of the half-width of the 22-GHz water vapor line on retrievals of temperature and
476 water vapor profiles with a 12-channel microwave radiometer. *IEEE Transactions*
477 *on Geoscience and Remote Sensing*, 43, 1102 – 1108.

478 Schultz, D. M., and R. J. Trapp (2003), Nonclassical cold-frontal structure caused by dry
479 subcloud air in Northern Utah during the intermountain precipitation experiment
480 (IPEX). *Mon. Wea. Rev.*, 131, 2222-2246.

481 Shaw, W. J., J. K. Lundquist, and S. Schreck (2009), Workshop on Research Needs for
482 Wind Resource Characterization. *Bull. Amer. Meteor. Soc*, 90, 535-538, doi:
483 10.1175/2008BAMS2729.1

484 Solheim, F., J. Godwin, and R. Ware (1998a), Passive ground-based remote sensing of
485 atmospheric temperature, water vapor, and cloud liquid water profiles by a
486 frequency synthesized microwave radiometer, *Met. Z.*, 7, 370-376.

487 —————, —————, E. Westwater, Y. Han, S. Keihm, K. Marsh, and R. Ware
488 (1998b), Radiometric profiling of temperature, water vapor and cloud liquid water
489 using various inversion methods, *Radio Science*, 33, 393-404.

490 Steenburgh, W. J., (2003), One hundred inches in one hundred hours: evolution of a
491 Wasatch Mountain winter storm cycle. *Wea. and Forecasting*, 18, 1018-1036.

492 Tindal A. C. Johnson, M. LeBlanc, K. Harman, E. Rareshide, and A. Graves, (2008),
493 Site-specific adjustments to wind turbine power curves, Proceedings of AWEA
494 WINDPOWER Conference, Houston, TX.

495 Vanderwende, B. and J. K. Lundquist (2011), The effects of atmospheric stability and
496 wind shear on wind farm power production, In review at *Wind Energy*.

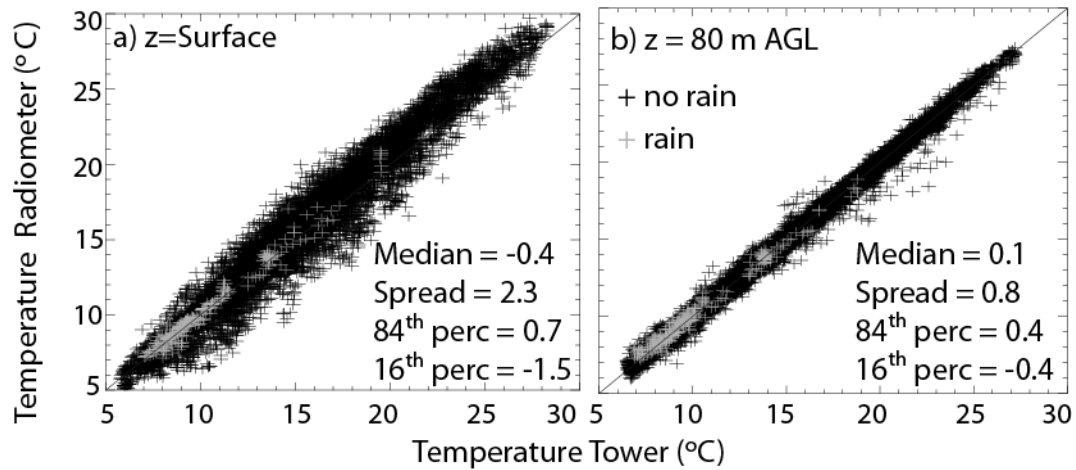
497 Vickers, D. and L. Mahrt (2004), Evaluating formulations of stable boundary layer
498 height. *J. Appl. Meteor.*, 43, 1736-1749

499 Wharton, S. and J. K. Lundquist (2011), Assessing atmospheric stability and its impacts
500 on rotor-disk wind characteristics at an onshore wind farm, Accepted for
501 publication at *Wind Energy*, DOI: 10.1002/we.483

502 Wisner, R. and M. Bolinger (2011), 2010 Wind technologies market report, pp.84, LBNL-
503 4820E, Berkeley, California: Lawrence Berkeley National Laboratory.

504

505



506

507

Figure 1: Scatter plot of temperature measured by thermometers mounted on a

508

meteorological tower and a microwave radiometer at a) the surface and b) 80 m AGL

509

between 24 May and 16 June 2011 (14141 samples = 235 hours, 41 minutes). Radiometer

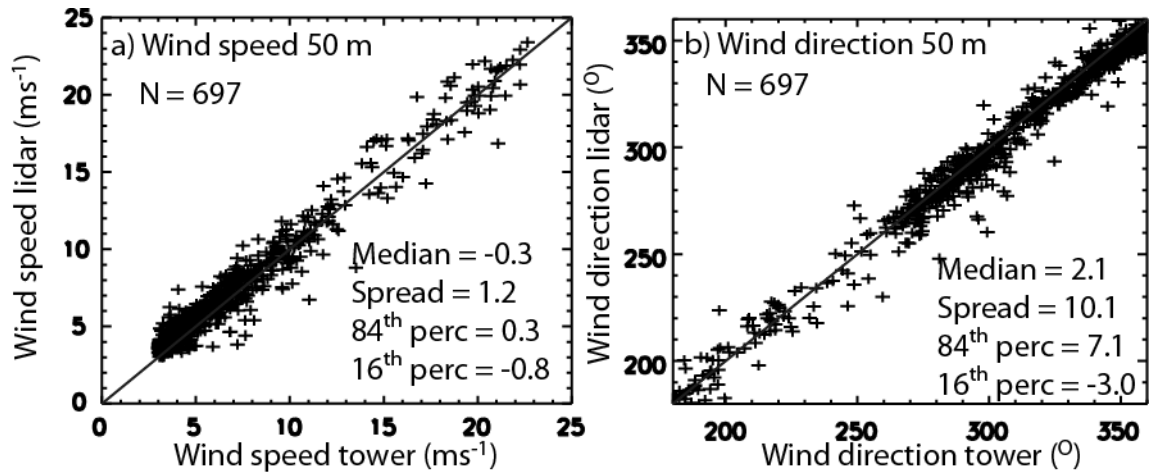
510

observation in b) were interpolated to 80 m using the 50 m and 100 m measures.

511

Measurements during rain are indicated in gray (518 samples = 8 hours, 38 minutes).

512



513

514 Figure 2: Scatter plot of a) wind speed and b) wind direction at 50 m AGL measured by

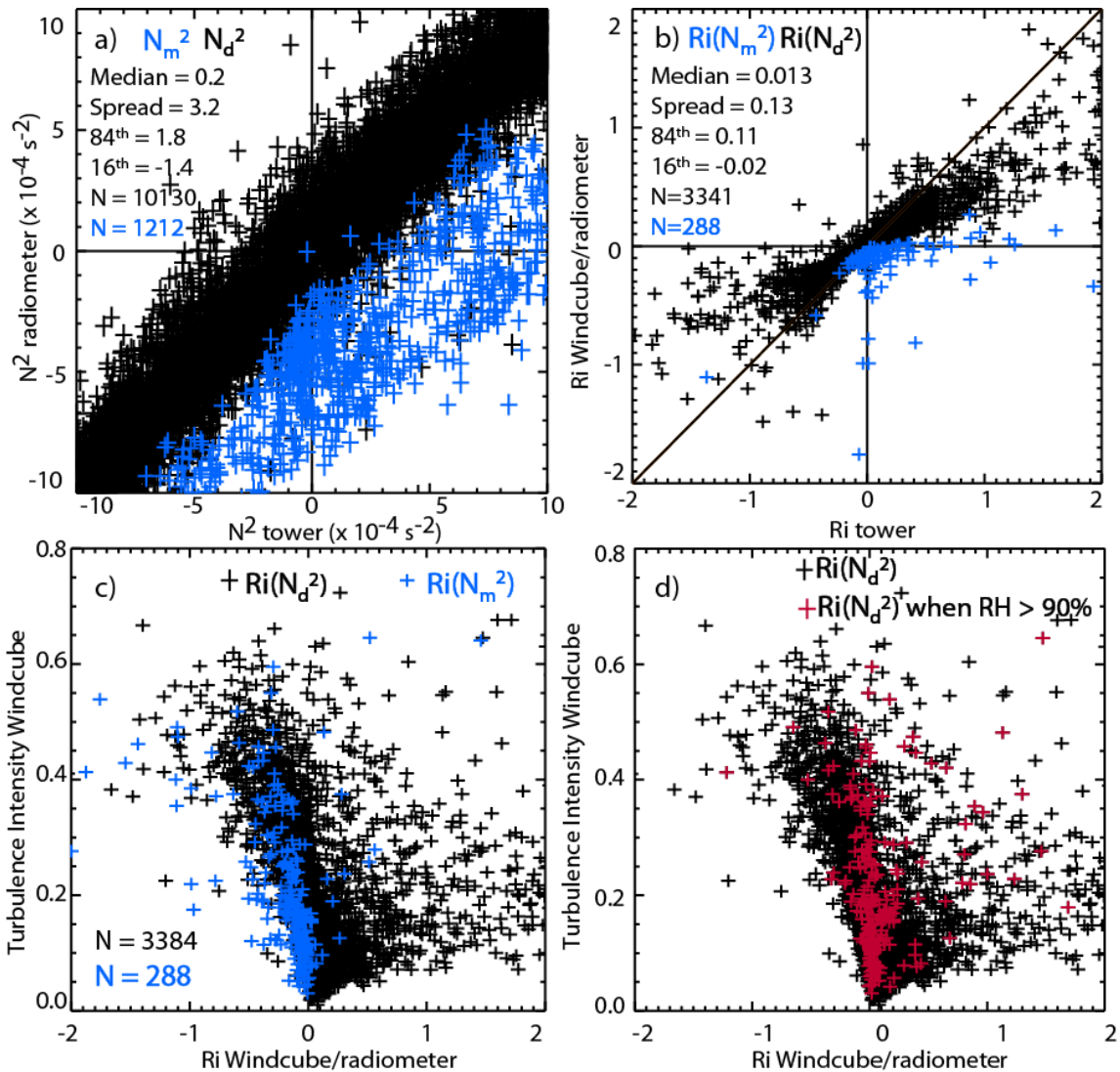
515 anemometers mounted on the meteorological tower and the Windcube lidar between 24

516 May-16 June 2011. Number of samples are indicated in a) and b).

517

518

519



520

521 Figure 3: a) Scatter plot of Brunt-Väisälä frequency for dry (black plus signs) and moist-

522 adiabatic conditions (blue plus signs) derived from 1-minute temperature observations at

523 the tower and 1-minute temperature and moisture measurements from the radiometer

524 between the surface and 80 m AGL. b) Scatter plot of the Richardson numbers between

525 the surface and 50 m AGL (black plus signs) measured by the anemometers and

526 Windcube lidar every 10 min. Black plus signs indicate the Richardson numbers using

527 the squared dry Brunt-Väisälä frequency, while blue plus signs represent the Richardson

528 numbers with the squared moist Brunt-Väisälä frequency. c-d) Turbulence intensity as a

529 function of Richardson numbers at 80 m AGL derived from the 10-minute Windcube
530 observations. Blue plus signs in c) represent time steps with moist-adiabatic conditions,
531 red plus signs in d) represent the same time steps but using the dry Richardson number.
532

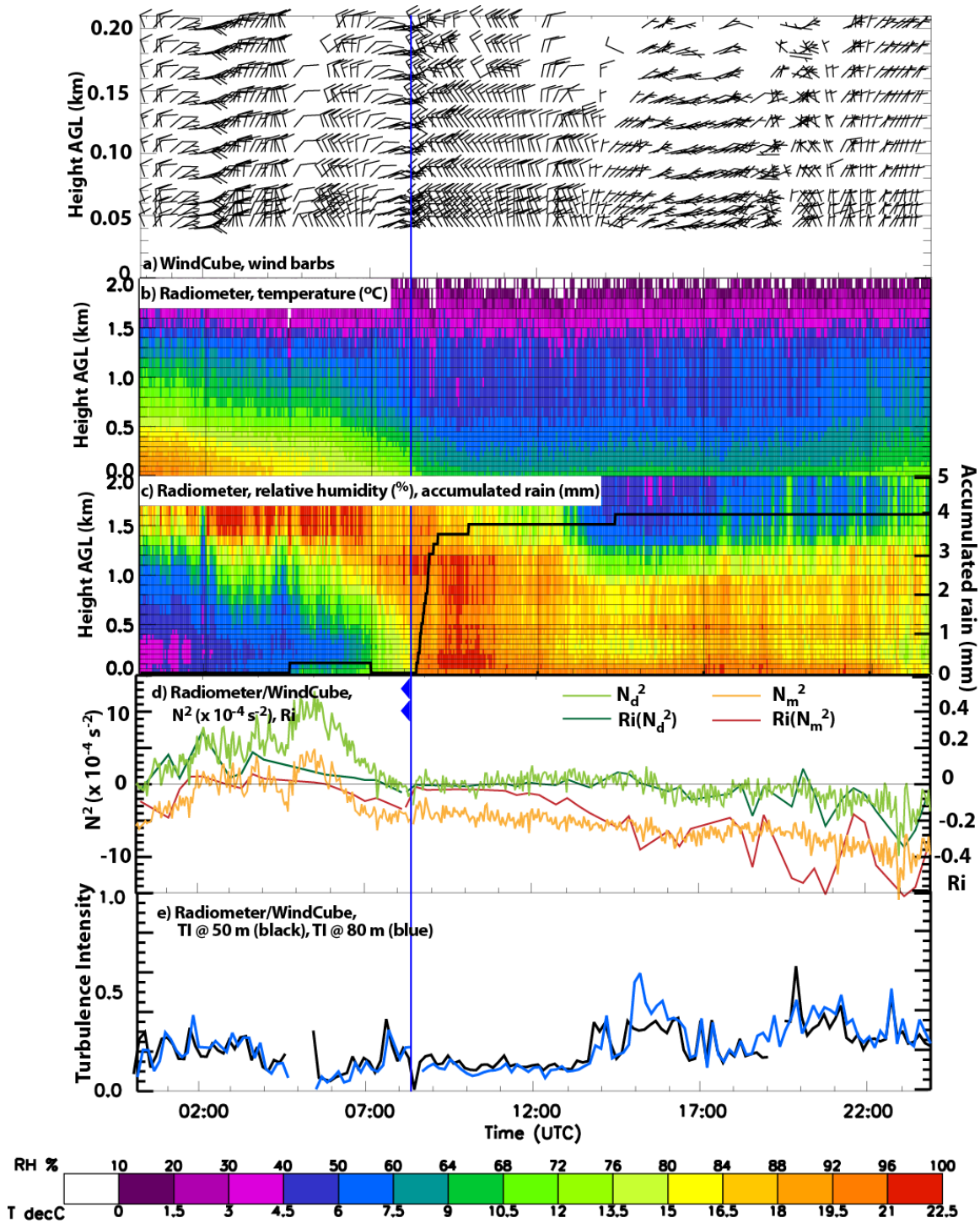


Figure 4: Windcube lidar and microwave observations on 9 June 2011 during a cold front passage. a) winds (half barb is 2.5 m s^{-1} and full barb is 5 m s^{-1}) observed by the Windcube lidar, b-c) temperature and relative humidity observed by the microwave

537 radiometer, d) moist and dry Brunt-Väisälä frequency between the surface and 50 m AGL
538 derived from radiometer observations and Richardson number derived from the
539 Windcube and radiometer measurements, and e) Turbulence intensity derived from the
540 Windcube lidar at 50 m and 80 m AGL. The location of the surface cold front is shown as
541 a blue line with filled triangle symbols attached. Rain was observed at the surface was
542 occasionally observed by the rain gauge at the tower.
543